

New apatite-type oxide ion conductor, $\text{Bi}_2\text{La}_8[(\text{GeO}_4)_6]\text{O}_3$: Structure, properties and direct imaging of low-level interstitial oxygen atoms using aberration-corrected scanning transmission electron microscopy

Matthew L. Tate,^{a,b} Douglas A. Blom,^c Maxim Avdeev,^b Helen E. A. Brand,^d Garry J. McIntyre,^b Thomas Vogt^e and Ivana Radosavljevic Evans^{a,b,}*

^a Durham University, Department of Chemistry, Science Site, South Road, Durham, DH1 3LE, UK

^b Australian Nuclear Science and Technology Organisation, Lucas Heights NSW 2234, Australia

^c Department of Chemical Engineering and NanoCenter, University of South Carolina, Columbia, SC 29208, USA

^d Australian Synchrotron, 800 Blackburn Road, Clayton VIC 3168, Australia

^e Department of Chemistry and Biochemistry and NanoCenter, University of South Carolina, Columbia, SC 29208, USA

Keywords: Ionic Conductors, Synchrotron and Neutron Diffraction, Scanning Transmission Electron Microscopy

The new solid electrolyte $\text{Bi}_2\text{La}_8[(\text{GeO}_4)_6]\text{O}_3$ has been prepared and characterized by variable-temperature synchrotron X-ray and neutron diffraction, aberration-corrected scanning transmission electron microscopy and physical property measurements (impedance spectroscopy and second harmonic generation). The material is a triclinic variant of the apatite structure type and owes its ionic conductivity to the presence of oxide ion interstitials. A combination of annular bright-field scanning transmission electron microscopy experiments and frozen-phonon multi-slice simulations enabled direct imaging of the crucial interstitial oxygen atoms present at a level of 8 out of 1030 electrons per formula unit of the material, and crystallographically disordered, in the unit cell. Scanning transmission electron microscopy also led to a direct observation of the local departures from the centrosymmetric average structure determined by diffraction. As no second harmonic generation signal was observed, these displacements are non-cooperative on the longer length scales probed by optical methods.

1. Introduction

Oxide ion conductors are technologically important materials owing to their applications in oxygen sensors and pumps, as catalysts and oxygen-separation membranes, and as electrolytes in solid oxide fuel cells (SOFCs). Apatite-type materials, particularly lanthanum germanates and silicates, show high oxide ion conductivities in the intermediate-temperature SOFC region (500 to 650°C).^[1-12] In some apatite materials, oxide ion conductivity occurs via vacancy-hopping,^[13] but in recent years increasing numbers of materials have been reported to exhibit an interstitial oxide conductivity mechanism.^[14-17] The locations of the interstitial oxide ions and the conductivity pathways in different apatite-type solid electrolytes are still debated in the literature.^[7, 14-26]

Apatite-type materials have the general formula $A_{10}(TO_4)_6X_{2\pm\delta}$, (A = alkaline or rare earth, Pb, Bi etc.; T = Ge, P, Si, V; X = halides, O, OH). This formula can be expressed as $[A^I_4][A^{II}_6][(TO_4)_6][X_2]$, reflecting the two distinct sites occupied by the A cations.^[27] This represents the apatite structure as a $[A^I_4][(TO_4)_6]$ framework made from columns of face-sharing $A^I O_6$ distorted trigonal prisms corner-connected to TO_4 tetrahedra, forming cavities along the [001] direction which accommodate $A^{II} X_2$ units (Figure 1).

Most known apatite-type materials are hexagonal, crystallising in space group $P6_3/m$.^[28] The remainder have monoclinic or triclinic structures, as reported for several cases in recent years^[2, 18, 29, 30] The origin of the triclinic distortion is thought to be the flexible nature of the $[A^I_4][(TO_4)_6]$ framework. If the framework is large relative to the $A^{II} X_2$ unit, the $A^{II}-O$ bonds undergo expansive stress, whilst the T-O bonds undergo compressive stress. To relieve this stress, tilting of the TO_4 tetrahedra occurs, in addition to a rotation of the triangular faces of the $A^I O_6$ trigonal prisms by the metaprism twist angle, ϕ . The twist angle is usually between 5 and 25°, with a larger twist angle corresponding to a greater size mismatch between the $A^{II} X_2$ cavity unit and the $[A^I_4][(TO_4)_6]$ framework; a material with a large twist angle is more likely to adopt a lower symmetry structure than hexagonal.^[27] The presence of interstitial oxide ions in apatite-type materials has been shown to promote the triclinic distortion, potentially by

further expansion of the framework.^[18, 29] The properties of apatites depend on their symmetry and the interstitial oxygen atoms, hence the reliable determination of the location of interstitials and the understanding of symmetry-lowering in these materials is of high importance.

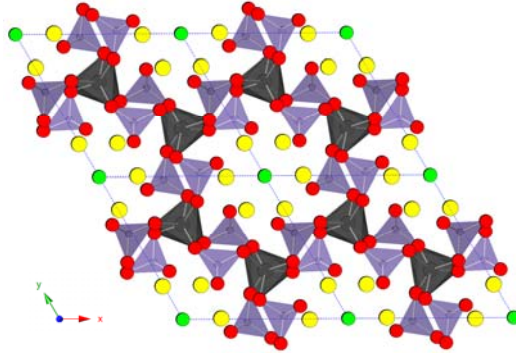


Figure 1. Projection of the $[A^I_4][A^{II}_6][(TO_4)_6][X_2]$ apatite structure down the c -axis. The atomic sites shown are: $[A^I]$ = black, $[A^{II}]$ = yellow, T = purple, O = red, X = green. Bonds within the $A^{II}_6X_2$ units have been omitted for clarity.

Recently, annular bright-field scanning transmission electron microscopy (ABF STEM) has emerged as a technique which allows the location and quantification of low-atomic number (Z) elements in close proximity to heavier atoms without the contrast reversals typically seen in HRTEM and conventional bright-field STEM.^[31] Hydrogen atoms have been imaged in β -NbH, characterized by a typical H:Nb ratio of 0.7 to 1.1.^[32] ABF STEM has been used to elucidate the rotation of BO_6 octahedra within perovskite interface materials,^[33] and for direct imaging of periodic anion vacancy ordering for a number of perovskites. For example, ABF STEM images for $La_{1-x}Sr_xCoO_{3-\delta}$ show an alternating arrangement between fully-occupied CoO_2 and anion-deficient $CoO_{2-\delta}$ layers,^[34] whilst for $SrMnO_{2.6}$, direct imaging of c -axis-aligned columns of O vacancies was achieved.^[35] Imaging with bright-field STEM has also been reported for $Nd_8Sr_2[(SiO_4)_6]O_2$, an apatite material without interstitial oxygen.^[36] However, despite their functional importance, direct imaging of low-level interstitial oxygen atoms has not been reported in the literature. Work by Zhang *et al.* used high-resolution transmission electron microscopy (HRTEM) on $La_8Sr_2[(SiO_4)_6]O_2$ and $La_9Sr[(SiO_4)_6]O_{2.5}$ to demonstrate indirectly the presence of interstitial oxygen atoms, and found that randomly distributed dark spots were observed in

the images for the latter material that were not seen in images for the former.^[37] These dark spots were attributed to interstitial oxygen atoms causing lattice distortion on a local scale. Dark regions within HRTEM images were also reported for the perovskite-type $\text{La}_4\text{Sr}_8\text{Ti}_{12}\text{O}_{38}$,^[38] caused by randomly distributed local defects due to the introduction of interstitial oxygen, but the interstitial oxygen atoms could not be directly observed.

In this paper, we report the preparation, structural characterization and physical properties of the new solid electrolyte $\text{Bi}_2\text{La}_8[(\text{GeO}_4)_6]\text{O}_3$, which adopts a triclinic apatite-type structure and undergoes a reversible phase transition to the hexagonal apatite aristotype at high temperature. The structure has been determined by a combination of synchrotron X-ray and neutron powder diffraction and ABF STEM. Crucially, low-level interstitial oxygen atoms, which play a key role in the oxide ion migration mechanisms in apatites and other types of fast ion conductors, have been directly imaged for the first time.

2. Results and Discussion

2.1. $\text{Bi}_2\text{La}_8[(\text{GeO}_4)_6]\text{O}_3$: Initial Structure Determination Heading

$\text{Bi}_2\text{La}_8[(\text{GeO}_4)_6]\text{O}_3$ is the first Bi(III)-containing apatite-type material with a triclinic structure reported to-date. Attempts to fit a hexagonal apatite structural model to the room-temperature data during the initial Rietveld analysis^[39] were unsuccessful; peak splitting was observed in the diffraction patterns which could not be accounted for by hexagonal symmetry. Rietveld fitting of the pattern was therefore performed using a triclinic structural model in space group $\text{P}\bar{1}$, previously reported for $\text{La}_{9.75}(\text{GeO}_4)_6\text{O}_{2.62}$. Note that this structural model is incomplete and corresponds to the formula, i.e. $\text{La}_{9.75}(\text{GeO}_4)_6\text{O}_2$, since the interstitial oxide ions were not located.^[29]

The cation fractional coordinates and site occupancies were first refined using the synchrotron PXRD data, with Bi and La initially distributed over all five unique A sites. Mixed La:Bi occupancy was found on all three A^{II} sites (in a 2:1 ratio, Table S2), while the A^{I} sites were found to contain La only. The

determination of the cation arrangement was followed by the analysis of the oxygen atom sublattice using the neutron powder diffraction (PND) data. Following the refinement of the “O26 model” ($\text{Bi}_2\text{La}_8[(\text{GeO}_4)_6]\text{O}_2$), difference Fourier maps were generated using the PND data to locate the additional nuclear density arising from the interstitial oxygen content (Figure 2). The strongest residual nuclear density peak was found at (0.5, 0.5, 0), the inversion center between the neighboring GeO_4 tetrahedra; this location corresponds to the brightest feature in Figure 2a. However, a better fit and a more plausible structural model was produced when this site was split, with interstitial oxygen atoms residing either side of the inversion center in the middle of the xy face, at $\sim (0.475, 0.510, 0.024)$. The next strongest residual density peak (weaker feature in Figure 2a, at $\sim (0.50826, 0.89497, 0.93865)$) and ultimately the remaining four similar sites which are independent in the triclinic structure, but become symmetry equivalents (6g) in the hexagonal apatite aristotype, were also considered as possible locations for interstitial oxygen. Refinements were carried out with these six sites occupied one at a time and simultaneously, with and without restraints on the overall oxygen content and with different treatment of the atomic displacement parameters (independent vs. equated). The conclusion from this systematic analysis was that, while the powder diffraction data contains some information about the excess oxygen content, they were insufficiently sensitive to reliably determine its distribution over all possible interstitial sites.

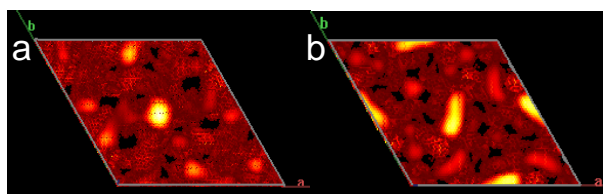


Figure 2. Difference Fourier maps for $\text{Bi}_2\text{La}_8[(\text{GeO}_4)_6]\text{O}_3$, derived from the PND data, viewed down the c -axis at: a) room temperature, b) 830°C.

The final combined PND and synchrotron PXRD data analysis, in which all atomic fractional coordinates and isotropic atomic displacement parameters were varied, was carried out with interstitial oxygen located only on the strongest residual nuclear density peak. This was the only model which gave

physically plausible values for bond lengths and angles around the defect and the isotropic atomic displacement parameters. However, it should be noted that this model is only approximate, and that the true distribution of the interstitial oxide ions in $\text{Bi}_2\text{La}_8[(\text{GeO}_4)_6]\text{O}_3$ is more complex. The Rietveld fit to the room-temperature data is shown in Figure 3, while the fractional coordinates, bond lengths and angles are given in Tables S2, S3, and S4 in the ESI.

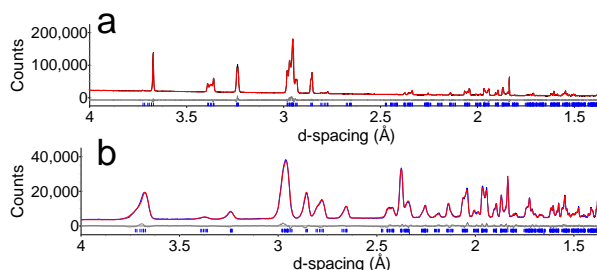


Figure 3. Rietveld fits to the room temperature: a) synchrotron PXRD data, b) PND data. $R_{wp} = 2.941\%$ (synchrotron PXRD), 4.344% (PND), 3.574% (combined). The PND pattern contains a small contribution from the Nb in the furnace heating elements.

Figure 4a shows this approximate model for room-temperature $\text{Bi}_2\text{La}_8[(\text{GeO}_4)_6]\text{O}_3$, with interstitial oxygen content located within the $[\text{A}^{\text{I}}_4][(\text{TO}_4)_6]$ framework and shown as orange spheres. Interstitial oxygen on site O5 results in the local formation of GeO_5 trigonal bipyramidal units, and the fractional occupancy of the O5 site is consistent with one GeO_4 tetrahedron per unit cell becoming a GeO_5 trigonal bipyramid, leading to an alternative formula $\text{Bi}_2\text{La}_8[(\text{GeO}_4)_5(\text{GeO}_5)]\text{O}_2$. These GeO_5 units are formed through distortion of the tetrahedra, to allow the interstitial oxygen atoms to occupy an axial site of the trigonal bipyramid. This distortion is evidenced by the O-Ge-O bond angles ranging from $76.6(9)$ to $124.1(4)^\circ$ (Figure S1 and Table S4 in ESI).

Using powder neutron diffraction, Pramana *et al.* also found the interstitial oxygen in triclinic $\text{La}_{10}[(\text{GeO}_4)_6]\text{O}_3$ within the $[\text{A}^{\text{I}}_4][(\text{TO}_4)_6]$ framework, but located on two positions close to $(0, 0.5, 0.5)$.^[18] This corresponds to the third-most-intense difference Fourier feature among the six sites we considered. By contrast, León-Reina *et al.* reported interstitial oxygen content within the walls of the cavities of $\text{La}_{9.6}[(\text{GeO}_4)_6]\text{O}_{2.4}$, at $(0.016(2), 0.228(2), 0.606(1))$.^[40]

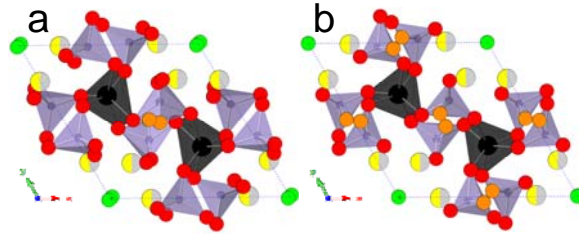


Figure 4. a) The triclinic room-temperature structure of $\text{Bi}_2\text{La}_8[(\text{GeO}_4)_6]\text{O}_3$ viewed down the z-axis. b) The hexagonal structure of $\text{Bi}_2\text{La}_8[(\text{GeO}_4)_6]\text{O}_3$ at 830°C viewed down the z-axis. $[\text{A}^{\text{I}}]$ (La) = black, $[\text{A}^{\text{II}}]$ (La/Bi) = yellow/grey, Ge = purple, O1-O3 = red, O4 = green, and O5 (interstitial) = orange.

The apparent ambiguity of the interstitial oxide ion location in triclinic apatite-type germanates and the inability to fully and reliably elucidate the distribution of oxide ions over possible interstitial sites in $\text{Bi}_2\text{La}_8[(\text{GeO}_4)_6]\text{O}_3$ by powder diffraction prompted us to undertake the STEM study.

3.2 $\text{Bi}_2\text{La}_8[(\text{GeO}_4)_6]\text{O}_3$: Direct Imaging of Interstitial Excess Oxygen Atoms and Local Departures from the Average Centrosymmetric Structure

To attempt direct observation of the interstitial oxygen atoms in $\text{Bi}_2\text{La}_8[(\text{GeO}_4)_6]\text{O}_3$ by ABF imaging, the same annular detector as used for high angle annular dark-field (HAADF) imaging was used to detect the outer parts of the bright-field (BF) diffraction disc which is more incoherent and indicates the location of atoms by dark shadows, including low Z atoms. This is in marked contrast to the inner parts of the BF diffraction disc which is dominated by phase contrast and therefore very dependent on thickness and focus conditions. While atomic columns in ABF images exhibit dark contrast on a bright background for most conditions relevant to experimental studies, making this imaging mode highly advantageous for locating oxygen in high-resolution images of oxide materials,^[41] the simple Z -contrast approximation used in HAADF no longer holds. Therefore, frozen-phonon multi-slice image simulations, which have been shown to match experimental ABF images of a variety of materials, are essential to guide experimental observations.

Using the model structure derived from the X-ray and neutron diffraction data as input, frozen-phonon multi-slice image simulations were performed for the [001] orientation of $\text{Bi}_2\text{La}_8[(\text{GeO}_4)_6]\text{O}_3$. The two A^{I} sites have a projected separation of 31 pm, well below the spatial resolution of the STEM and therefore all cations appear as a single “column” in the STEM simulations and experiments. Electron scattering from columns containing different kinds of atoms will vary depending on the detailed stacking order along the electron beam propagation direction.^[42] For the image simulation of the A^{II} sites containing both La and Bi, a simple random solution was assumed. The image simulation was performed for a thickness of 30 cations. It therefore follows that the Bi composition was quantised in 3.3 atomic % units. Since the Bi site occupancy in the model varied by less than that value, the image simulations were carried out with 10 Bi atoms and 20 La atoms in each A^{II} site arranged in a random fashion along [001]. For the interstitial oxygen in site O5, the 50% occupancy factor translates into 15 atoms of oxygen distributed among 30 potential sites for each of the two O5 projected sites in the unit cell.

Figure 5a shows the HAADF STEM image simulation for the [001] orientation of $\text{Bi}_2\text{La}_8[(\text{GeO}_4)_6]\text{O}_3$. The white parallelogram marks the unit cell in this projection (the a -axis is horizontal, as in Figure 1). The brightest features in the image simulation correspond to the two overlapped La A^{I} sites. The second-most-intense features correspond to the A^{II} mixed La/Bi sites. The T-site (T = Ge) columns have the weakest signal, while the oxygen columns are not visible in the HAADF image simulation. As expected, the two cations of the A^{I} sites are not resolved, although the feature is distinctly not spherical. The La-only A^{I} column image intensity is higher than the one with mixed La/Bi A^{II} due to the density of atoms along [001]. The A^{I} cations are spaced $c/2$ (3.67) Å apart, while the A^{II} cations repeat every c (7.35 Å). To facilitate quantitative comparison between the image simulations and experimental STEM images, we use the integrated signal over the projected atomic columns.^[43, 44] This method has been shown to be insensitive to small focus changes and the incoherent broadening the simulations typically need to match the pixel-by-pixel intensities of experimental data. An area associated with each atomic

site in the image simulation with a radius of 4.5 pixels (43.2 pm) was selected and the signal inside the area was integrated to measure the scattering at each site.

Figure 5b shows the simulated signal from the various cation projected sites. The HAADF signal is dominated by thermal diffuse scattering and is therefore sensitive to the ADPs of the atoms. The minor differences in the simulated HAADF intensities for the three tetrahedral T sites and the three La/Bi mixed sites are due to the varying atomic displacement parameters (ADPs) in the model structure obtained by Rietveld refinement, which contain both systematic and random errors. However, as shown in Figure 5 and described below, the intensity values of individual site types correspond well to the experimentally observed ones. Stacking variations resulted in a negligible change in the integrated image intensities.

Figure 5c shows the experimental HAADF micrograph along [001]. The cation sites are all evident in the image, while the oxygen sites are not apparent. In Figure 5c there are approximately 200 different atomic columns of each of the 7 cation sites for a total of 1,368 atomic columns. The atomic columns were sorted into the corresponding types and the integrated signal for each different cation site was extracted and is plotted in Figure 5d. They fall into three broad groups: the A^I sites have the highest intensity, the A^{II} sites are next, followed by the considerably weaker T sites. The experimental evidence suggests that the compositions of the three A^{II} sites are identical with similar ADPs. The A^I sites overlap in this projection and appear as one column which is the most intense feature in the dataset as expected from the image simulations. The signals from all the T sites are consistent, suggesting that the composition and ADPs of these sites should be similar. Experimentally we do not observe the slight differences in the image intensities apparent in the simulations. Possible causes could be that the differences are smaller than the noise in the experimental images, and the relatively large standard uncertainties on the ADP values obtained by diffraction. The relative contrast differences between the various cation site types are smaller in the experiment than in the image simulations. This suggests that the experimental specimen was thicker than the simulated one.

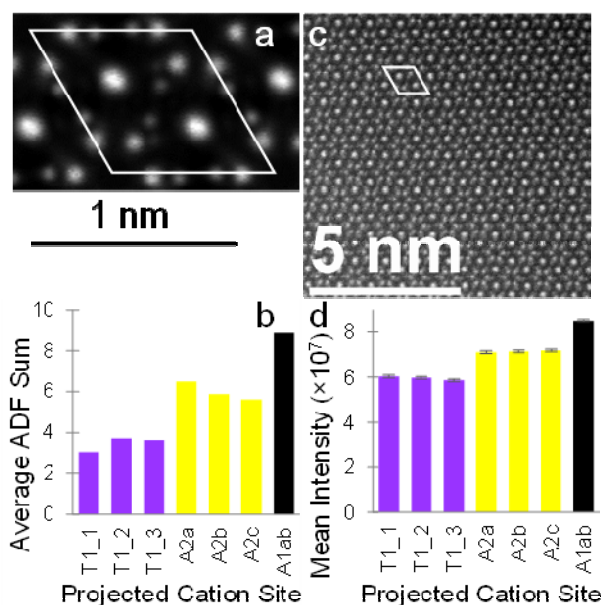


Figure 5. (a) HAADF STEM image simulation for [001] oriented of $\text{Bi}_2\text{La}_8[(\text{GeO}_4)_6]\text{O}_3$; (b) The signal extracted from the cation sites of the image simulation; (c) Experimental HAADF micrograph along [001] of $\text{Bi}_2\text{La}_8[(\text{GeO}_4)_6]\text{O}_3$; (d) Integrated signal for different cation sites. Error bars indicate the 95% confidence limits of the mean. Color coding of the graphs corresponds to the representation of the structure shown in Figure 1.

Figure 6 shows the ABF image simulation along [001]. An important part of ABF image simulation is to model the ‘machine parameters’ of the microscope in order to assure that one has the experimental setup to image lighter elements (in this case oxygen). Table S1 provides a summary of parameters that were used for the experiments after simulations had shown them to maximize the signal in both HAADF and ABF STEM imaging. The black parallelogram in Figure 6a marks the unit cell, with the *a*-axis horizontal, and the assignment of sites is shown in Figure 6b. In addition to the cation sites from the HAADF simulation, additional features are seen which correspond to some of the oxygen sites in the model structure based on diffraction. At the corners of the unit cell, the O4 site is clearly seen in the simulation. O1_1 and O2_1 are well-separated; O1_2 and O2_2 are evident in the simulated image, but not resolved; O1_3 and O2_3 also appear in the simulated image, but are not clearly resolved. O3_1 and O3_4 show strong contrast in the simulated ABF image near the A2b site. The O5 projected site lies nearly at the center of the unit cell outline but exhibits weak contrast in the simulation.

To test the significance of the intensity simulated at the O5 projected sites, two additional locations were used as intensity reference points; we refer to them as projected site X and projected site Y. X effectively corresponds to the second strongest feature observed in the difference Fourier map based on neutron diffraction data and is defined along the *a*-axis halfway between the Ge T1_3 sites; similarly, Y lies along the *b*-axis halfway between the Ge T1_2 sites, at *z*=0 and ½. The local surroundings for these sites are similar to the O5 sites, and in the ideal hexagonal apatite structure they are equivalent by symmetry. Integrated intensities for the various atomic projected sites were extracted from the ABF simulation as was done for the HAADF simulation. Figure 6c summarizes the results. Since the signal is reversed relative to the HAADF images, the site with the highest intensity has the lowest numerical integrated intensity.

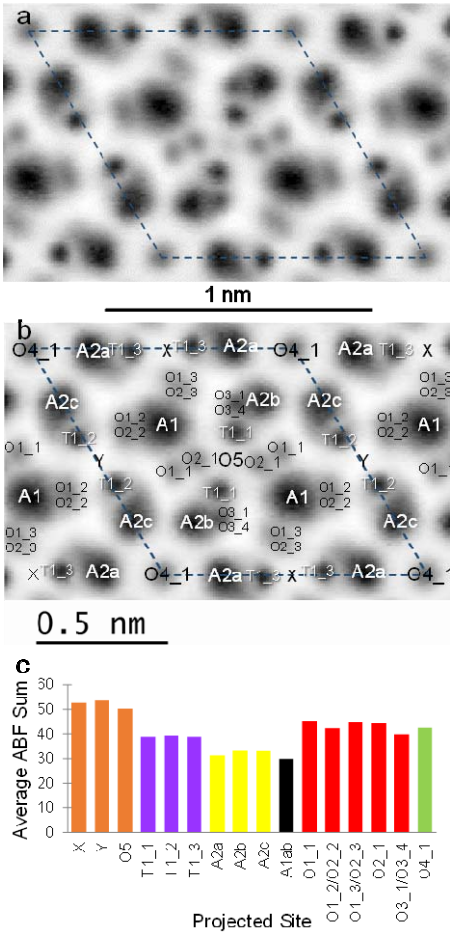


Figure 6. (a) ABF image simulation for the [001] orientation of $\text{Bi}_2\text{La}_8[(\text{GeO}_4)_6]\text{O}_3$; (b) The assignments of sites; (c) Integrated intensities for different projected cation and oxygen atom sites. Color coding of the graphs corresponds to the representation of the structure shown in Figure 1.

The A^{I} framework cations have the most-intense image intensity (the lowest bar height in Figure 6c) and are not resolved, as was noted for the HAADF data. The next-highest intensities correspond to the three A^{II} cations with a similar trend as observed for the HAADF simulations. The ABF signal for light elements is dominated by elastic scattering, while for higher atomic number species, the proportion of thermal scattering increases. Thicker samples will have more inelastic scattering as well.^[31] Variations of ADP will affect both the thermally-scattered electrons and change the channeling conditions for the elastically scattered electrons and lead to changes in the ABF signal. For heavy atoms like La and Bi the ABF signal includes a larger proportion of thermal scattering^[31] suggesting that the differences in the simulated ABF image are due to differences in the ADPs of the different sites in the model structure. All the T cations have indistinguishable intensities in the ABF image. For the lighter Ge atoms, the proportion of thermal scattering contributing to the ABF image is smaller and therefore the differences are not observed.

The signal from the different oxygen columns is much more variable than for the cations. Significant electron channeling is expected for most of the oxygen columns due to their close proximity to a much heavier cation site. The combined O3_1/O3_4 column exhibits stronger contrast than the other oxygen sites in similar proximity to the A^{II} cations. In the model structure, site O3_4 has a much smaller B_{iso} than the other O3 sites. The channeling conditions of the elastically scattered electrons depend on B_{iso} and explain the variation in the simulated ABF intensity.

The signals at the projected sites X and Y serve as a reference to compare the extremely low signal attributed to the interstitial oxygen O5 site. The simulation suggests that interstitial oxygen in the O5 site does contribute to measurable contrast. To explore further the signal at the O5 site, additional image simulations were performed. The same model structure was used, with the exception that no oxygen at the O5 position was included. Figure S2 is the difference image between the two simulations. The

speckles throughout the unit cell are indicative of the variability in the simulations for identical inputs. The difference is well localized at the projected location of the O5 site and shows reasonable contrast. The ABF image simulations therefore suggest that ABF STEM imaging should be sensitive enough to detect 50% occupancy of oxygen in the O5 site of the structure.

An experimental ABF image of $\text{Bi}_2\text{La}_8[(\text{GeO}_4)_6]\text{O}_3$ is shown in Figure 7a. All the projected atomic columns of the image simulation are apparent in the experimental image. The same quantitative analysis was performed as described earlier for the HAADF image. In this case there are approximately 300 examples of each atomic column. For each column type, a range of signal intensities was measured across the image. These should follow a normal distribution if the variation between different columns of the same type is due to random measurement error. Most of the cation columns were indeed normally distributed, but significant deviations were observed for Ge T1_1, La/Bi A2b, and Ge T1_3. To investigate this further, the analysis was also carried out without the symmetry constraints of the $P\bar{1}$ space group. Figure 7b summarizes the analysis for the centrosymmetric case, while Figure 7c is without enforcement of symmetry. In the latter case, most of the atomic projected sites still retain the expected centrosymmetry. However, for both Ge T1_1 and A2b projected sites (Figures S3a and S3b), the two subsets are clearly distinct and each subset is now normally distributed. The variability for the Ge site T1_3, while significant for a 1% t-test criterion, is much smaller than observed for the other cation sites which apparently violate centrosymmetry.

The ABF column intensities associated with oxygen that seemingly violate centrosymmetry (O3_1/O3_4 and O1_2/O2_2) are shown in Figures S3c and S3d. O3_1/O3_4 are closely associated with the Ge T1_1 sites. The Ge T1_1 site which appears darker in the ABF image is associated with the O3_1/O3_4 site which is lighter, suggesting perhaps transfer of O signal from the nominal O3_1/O3_4 site to be more overlapped with the projected location of the Ge T1_1 site. The O1_2/O2_2 sites face each other across site Y in the structure and are clearly distinct in the ABF data.

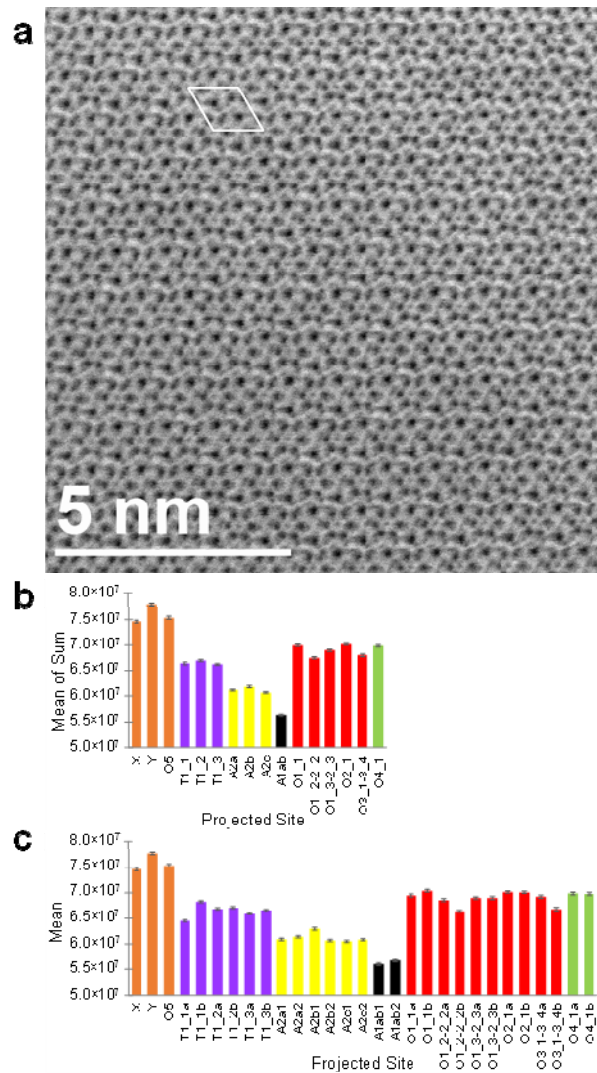


Figure 7. (a) Experimental ABF image for the [001] orientation of $\text{Bi}_2\text{La}_8[(\text{GeO}_4)_6]\text{O}_3$; (b) Integrated intensities for different cation and oxygen atom columns in $\text{P}\bar{1}$; (c) Integrated intensities for different cation and oxygen atom columns without the inversion center symmetry constraint. Error bars indicate the 95% confidence limits of the mean. Color coding of the graphs corresponds to the representation of the structure shown in Figure 1.

The key part of this analysis concerns the experimental integrated column intensities for O5, X and Y, and this indicates that columns X and O5 have essentially the same electron scatter, significantly more intense than that of Y (see Figures 7b and 7c where a darker contrast is a lower value on the y-axis). The result of the multi-slice simulations where the interstitial oxygen was in O5 and nothing was in X and Y, indicated that the latter two should be identical and brighter than O5. The histograms of these three

projected sites are seen in Figure 8. There is clearly more electron scattering density on X and O5 than observed for Y across the field of view in the ABF micrograph.

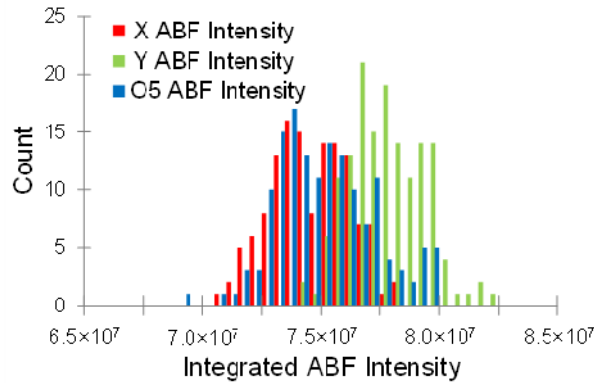


Figure 8. Integrated ABF intensities for projected sites X, Y and O5. A darker contrast results in a lower count in bright-field imaging.

We therefore conclude that we have successfully directly imaged low-level interstitial oxygen atoms in apatite-type $\text{Bi}_2\text{La}_8[(\text{GeO}_4)_6]\text{O}_3$ in two locations which give a combined content of one oxygen atom per formula unit. This extra electron adds 8 electrons to the 1022 electrons per formula unit of the material. To reliably locate and refine the contribution of the small additional scattering intensity in a material with a high degree of pseudo-symmetry using powder diffraction techniques is very challenging and the complementary use of real space STEM imaging demonstrated here is strongly encouraged. Furthermore, we have directly observed local-scale departures from the average centrosymmetric structure obtained by high-resolution diffraction methods. We note that no SHG signal was observed for this material. This indicates that the local deviations from centrosymmetric arrangements observed by ABF imaging are not cooperatively ordered on length-scales which would enable an SHG response. The SHG signal scales with $\sin^2(\text{thickness})$ of such a domain and might be at the limit of detectability.^[45]

3.3 Phase Transitions and Symmetry Lowering

Synchrotron PXRD and neutron powder diffraction data collected at 830°C were analysed in a similar fashion to the room-temperature data. The peak splitting observed at room temperature was not present and a hexagonal structural model could be used for the refinements. The interstitial oxygen atoms were located from the difference Fourier maps generated from neutron data, and somewhat smeared out residual nuclear density features were found centered around $\sim (0.482, 0.515, 0.023)$, Figure 2b. This crystallographic site corresponds to locations between all pairs of neighbouring GeO_4 tetrahedra (Figure 4b) and corresponds to sites O5, X and Y becoming crystallographically equivalent.

The Rietveld fits to the 830°C data sets are shown in Figure 9 and the fractional atomic coordinates, bond lengths and angles are given in Tables S5 and S6 in the ESI.

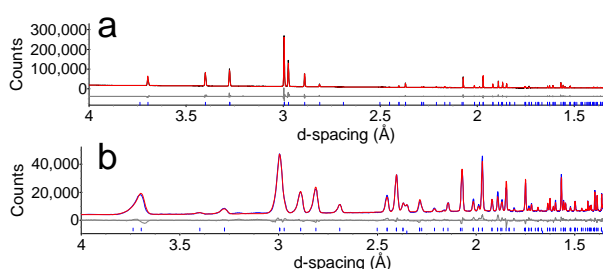


Figure 9. The final Rietveld fits to the 830°C data: a) synchrotron PXRD data, b) PND data. $R_{wp} = 3.999\%$ (synchrotron PXRD), 4.904% (PND), 4.439% (combined). The PND pattern contains a small contribution from the Nb in the furnace heating elements.

To investigate the phase transition between triclinic and hexagonal $\text{Bi}_2\text{La}_8[(\text{GeO}_4)_6]\text{O}_3$, Rietveld refinements were carried out on the variable-temperature synchrotron PXRD data, and the obtained lattice parameters are plotted in Figure 10. The triclinic material is stable up to 680°C, where it undergoes a reversible phase transition to the hexagonal form. Similar observations were reported for $\text{La}_{9.75}[(\text{GeO}_4)_6]\text{O}_{2.625}$ and $\text{La}_{10}[(\text{GeO}_4)_6]\text{O}_3$, which undergo phase transitions from triclinic to hexagonal structures at approximately 750°C and 850°C respectively.^[46, 47]

To determine whether the phase transition and the symmetry reduction in $\text{Bi}_2\text{La}_8[(\text{GeO}_4)_6]\text{O}_3$ on cooling can be ascribed to the need to reduce under-bonding on the A^I sites and over-bonding on the T sites

caused by differences in the size of the framework and the $A^{II}_6X_2$ units, as proposed by Baikie *et al.*,^[27] bond valence sums for the cations were calculated (Table S7). It appears that $\text{Bi}_2\text{La}_8[(\text{GeO}_4)_6]\text{O}_3$ does not fully follow this trend. Both A sites are under-bonded in the high-temperature hexagonal structure; in the room-temperature triclinic form, three out of five unique A sites remain under-bonded. Related to this, it is also reported that an increase in the metaprism twist angle, ϕ , reduces under- and over-bonding of sites, and results in a lower symmetry structure.^[27] The metaprism twist angles for the two forms of $\text{Bi}_2\text{La}_8[(\text{GeO}_4)_6]\text{O}_3$ were calculated using the method described by White *et al.*^[28] It was found that the average twist angle of $23.7(4)^\circ$ in the triclinic structure does not change significantly in the hexagonal form ($23.29(3)^\circ$). We therefore conclude that there is not a simple relationship between increasing the metaprism twist angle and symmetry lowering in $\text{Bi}_2\text{La}_8[(\text{GeO}_4)_6]\text{O}_3$.

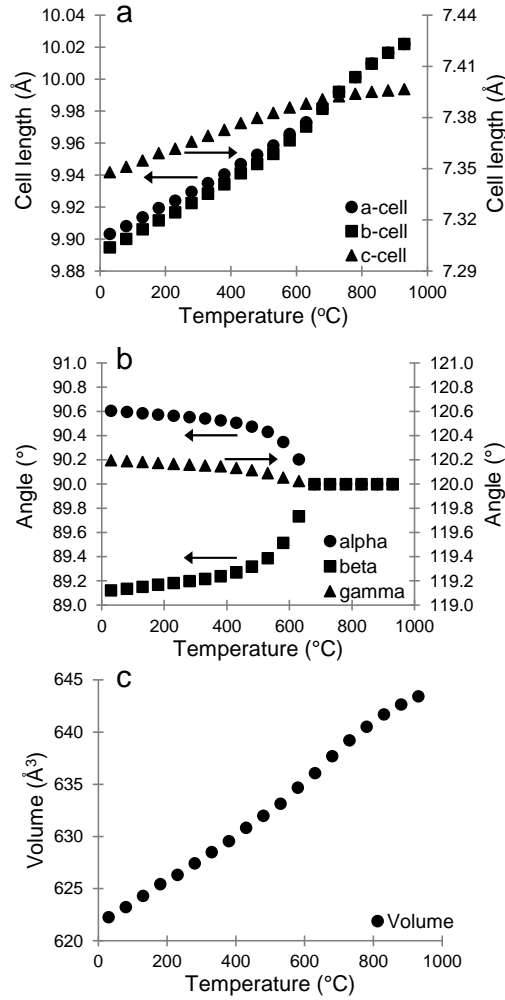


Figure 10. Variation of the unit cell parameters: a) a , b , and c -cell lengths, b) α , β , and γ angles, and c) unit cell volume with temperature for $\text{Bi}_2\text{La}_8[(\text{GeO}_4)_6]\text{O}_3$ from synchrotron PXRD data. The error bars are smaller than the data points.

3.4 Ionic Conductivity

AC impedance measurements were performed on heating from 300 to 800 $^{\circ}\text{C}$. At low temperatures, the complex impedance spectra show a large semi-circular arc, attributed to the bulk response, along with a Warburg-type electrode response at low frequencies. The bulk responses of the samples were treated using an equivalent circuit consisting of a parallel combination of a resistor and a capacitor, and the grain boundary response could not be distinguished from the bulk responses at high frequencies in the large impedance arc. The low-frequency intercepts of the large semi-circular arcs are due to the bulk resistivities of the sample, and the corresponding capacitance estimated from $\omega RC = 1$ (where $\omega =$

$2\pi f_{max}$, f_{max} being the frequency at the maximum imaginary impedance for the semicircular arc, Z''_{max} at 300°C is 3.66 pFcm⁻¹, consistent with a bulk response. At low frequencies (below 10 Hz), the capacitance from the Warburg-type electrode response is between 10⁻⁷ and 10⁻⁵ Fcm⁻¹, indicative of ionic conduction.^[48]

The conductivity of Bi₂La₈[(GeO₄)₆]O₃ between 300 and 800°C, along with those for yttria-stabilised zirconia (Zr_{0.92}Y_{0.08}O_{1.92}), and La₁₀[(GeO₄)₆]O₃ are shown in Figure 11. The activation energy is 1.44 eV between 530 and 725°C, comparable to that of in the same temperature region.^[49]

Bi₂La₈[(GeO₄)₆]O₃ is a good oxide ion conductor, with a conductivity slightly lower than that of La₁₀[(GeO₄)₆]O₃, reaching 0.01 Scm⁻¹ at 800°C. This could be due to the lone pairs on the Bi³⁺, which are thought to occupy partially the cavity containing the O4 oxide ions (green spheres in Figure 4), thereby hindering their intra-channel mobility.^[49]

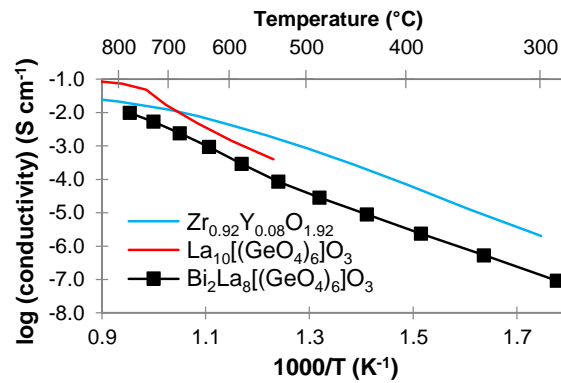


Figure 11. Arrhenius plots of total conductivity for Bi₂La₈[(GeO₄)₆]O₃, La₁₀[(GeO₄)₆]O₃,^[49] and Zr_{0.92}Y_{0.08}O_{1.92}.^[14]

Conclusion

A new solid electrolyte Bi₂La₈[(GeO₄)₆]O₃ has been prepared and characterized by variable-temperature synchrotron X-ray and neutron diffraction, aberration-corrected scanning transmission electron microscopy, impedance spectroscopy and second harmonic generation measurement. At room temperature the material adopts a triclinic structure in space group $P\bar{1}$, and it undergoes a reversible

phase transition into the archetypal hexagonal apatite structure (space group P63/m) near 680°C.

$\text{Bi}_2\text{La}_8[(\text{GeO}_4)_6]\text{O}_3$ owes its ionic conductivity to the presence of oxide ion interstitials.

Annular bright-field scanning transmission electron microscopy (ABF STEM) experiments underpinned by frozen-phonon multi-slice simulations enabled us to image directly the interstitial oxygen atoms present at a level of 8 out of 1030 electrons in the unit cell (i.e. 0.8% of total electron content). STEM also led to a direct observation of local departures from a centrosymmetric average structure determined by X-ray and neutron diffraction. However, no second harmonic generation signal was observed from this material, suggesting that these displacements are non-cooperative at longer length scales probed by diffraction methods. Such local displacements could potentially be due to the A-cation distribution and the Bi^{3+} lone-pair effects. As there is only one Bi^{3+} for every two La^{3+} in random stacking order the ordered domains will be small and disconnected. Nevertheless, it appears that a minute local asymmetry can be created which is detectable by ABF imaging of small domains. Our ongoing and future work, which will shed more light on this, includes density functional theory (DFT) calculations and lone-pair localisation, as well as variable-temperature synchrotron and neutron total scattering and pair distribution function (PDF) analysis of the local structure.

The results presented here demonstrate that very low levels of crystallographically disordered interstitial oxygen atoms can be directly imaged successfully by ABF-STEM. This will have a significant and broad impact on understanding the structure-property relationships in functional oxides where properties are intrinsically linked to interstitials and defects.

Experimental Section

Sample preparation

Polycrystalline $\text{Bi}_2\text{La}_8[(\text{GeO}_4)_6]\text{O}_3$ was synthesized by a high-temperature solid-state reaction using Bi_2O_3 (Sigma-Aldrich, 99.9 %), GeO_2 (Sigma-Aldrich, 99.99 %) and La_2O_3 (Sigma-Aldrich, 99.9 %, dried at 1000°C overnight before use) as reagents. A stoichiometric ratio of the reagents was ground and

fired in an alumina crucible at 1100°C (30 hrs, with intermittent grinding), with heating and cooling rates of 5°C per minute.

A portion of the powdered sample was uniaxially pressed into a pellet (diameter of ~1 cm and thickness of ~0.1 cm) and sintered at the synthesis temperature for 6 hrs for electrical characterization.

Powder X-ray and neutron diffraction

To assess sample purity, room-temperature powder X-ray diffraction (PXRD) data were collected on a Bruker AXS D8 Advance diffractometer using Cu K α radiation and equipped with a Lynx-Eye detector. Synchrotron PXRD data were collected on the Powder Diffraction Beamline at the Australian Synchrotron.^[50] The sample was finely ground and placed into a 0.2 mm diameter quartz capillary which was rotated during data collection. Variable-temperature PXRD (VT-PXRD) data were collected between 30°C and 930°C on heating and between 880°C and 30°C on cooling, in temperature intervals of 50°C, using a Cyberstar hot-air blower attachment. Data were collected in a 2θ range of 3 to 83 ° using a monochromated X-ray beam ($\lambda = 0.6354$ Å, calibrated against NIST SRM660b LaB₆) and a Mythen II microstrip detector. Each data set was collected with the detector in two different positions offset by 0.5 ° to cover gaps in the angular range of the modular detector strip, with a collection time of 900 seconds per position. The two collected data sets were then combined into a single diffraction pattern using the PDViPeR software.

Neutron diffraction data were collected on the ECHIDNA powder neutron diffractometer on the OPAL reactor at ANSTO,^[51] between 30°C and 830°C on heating and 730°C to 130°C on cooling in temperature intervals of 100°C, using a vacuum furnace with a niobium heater. Approximately 7 g of powdered sample was placed into a 9 mm diameter vanadium can and data were obtained over the 2θ range of 6 to 164 °, with the wavelength of the neutrons fixed at 2.4395(5) Å using the [331] reflection of a germanium monochromator. No additional collimation was applied. All powder diffraction data were analysed using the Topas Academic software.^[52] The Durham in-house multitopas routine was

used to analyse the data collected from the variable-temperature experiments and extract the lattice parameters for $\text{Bi}_2\text{La}_8[(\text{GeO}_4)_6]\text{O}_3$.^[53]

AC impedance spectroscopy

AC impedance spectroscopy measurements were performed in air using a Solartron 1260 frequency response analyser over a 10^6 to 10^{-1} Hz frequency range. The circular faces of the sintered pellet were coated with a fine layer of platinum paste and affixed atop a Probostat A-6 cell, then fired at 800°C for 1 hr to eliminate the organic components from the paste to form platinum electrodes. The impedance data were collected on heating from 300 to 800°C in temperature intervals of 50°C , with a heating rate of $5^\circ\text{C}/\text{min}$. Prior to data collection, the pellet was thermally stabilised for 45 mins. The complex impedance data were analysed using the Zview 3.0a software package.

Second harmonic generation (SHG) test

SHG measurements were conducted using a modified Kurtz-NLO system with a 1064 nm light source. The 532 nm SHG was collected in reflection and detected using a photomultiplier tube. A 532 nm narrow-bandpass interference filter was attached to the tube in order to detect only SHG light.^[54]

Scanning transmission electron microscopy and frozen-phonon simulations

Aberration-corrected scanning transmission electron microscope (AC-STEM) data in both the Z-contrast high angle annular dark-field (HAADF) and annular bright-field (ABF) imaging modes were collected from the powdered $\text{Bi}_2\text{La}_8[(\text{GeO}_4)_6]\text{O}_3$ samples. The powder was lightly ground in an agate mortar and pestle before loading onto holey carbon-coated Cu TEM grids. A JEOL JEM2100F with a CEOS aberration corrector for the electron probe was used at 200 kV to image the sample. Frozen-phonon STEM image simulations were done using the multi-slice code of Kirkland.^[55] The parameters of the image simulations and experimental STEM data collection are listed in Table S1 in the electronic supplementary information (ESI) file.

Acknowledgements

The authors thank Durham University and ANSTO for a PhD studentship for MLT. IRE and TV thank ANSTO for support as visiting researchers. We thank Prof. Shiv Halasyamani (University of Houston) for the SHG measurements. The authors acknowledge the Research Cyberinfrastructure (RCI) program under the Office of Information Technology and Vice President for Research at the University of South Carolina contributed to the results in this paper by providing High Performance Computing resources. Part of this research was undertaken on the Powder Diffraction beamline at the Australian Synchrotron.

References

- [1] P. R. Slater, J. E. H. Sansom, J. R. Tolchard, *Chemical Record* **2004**, 4, 373.
- [2] A. Orera, T. Baikie, P. Panchmatia, T. J. White, J. Hanna, M. E. Smith, M. S. Islam, E. Kendrick, P. R. Slater, *Fuel Cells* **2011**, 11, 10.
- [3] H. Li, T. Baikie, S. S. Pramana, J. F. Shin, P. R. Slater, F. Brink, J. Hester, K. Wallwork, T. J. White, *Journal of Materials Chemistry* **2012**, 22, 2658.
- [4] L. León-Reina, E. R. Losilla, M. Martínez-Lara, S. Bruque, A. Llobet, D. V. Sheptyakov, M. A. G. Aranda, *Journal of Materials Chemistry* **2005**, 15, 2489.
- [5] H. Zhang, F. Li, J. Jin, Q. Wang, Y. Sun, *Solid State Ionics* **2008**, 179, 1024.
- [6] H. Li, T. Baikie, S. S. Pramana, J. F. Shin, P. J. Keenan, P. R. Slater, F. Brink, J. Hester, T. An, T. J. White, *Inorganic Chemistry* **2014**, 53, 4803.
- [7] L. León-Reina, J. M. Porras-Vazquez, E. R. Losilla, M. A. G. Aranda, *Solid State Ionics* **2006**, 177, 1307.
- [8] J. McFarlane, S. Barth, M. Swaffer, J. E. H. Sansom, P. R. Slater, *Ionics* **2002**, 8, 149.
- [9] S. P. Jiang, L. Zhang, H. Q. He, R. K. Yap, Y. Xiang, *Journal of Power Sources* **2009**, 189, 972.
- [10] J. Xiang, Z.-G. Liu, J.-H. Ouyang, F.-Y. Yan, *Journal of Power Sources* **2014**, 251, 305.
- [11] H. Yoshioka, S. Tanase, *Solid State Ionics* **2005**, 176, 2395.
- [12] J. E. H. Sansom, P. R. Slater, *Solid State Ionics* **2004**, 167, 23.
- [13] J. R. Tolchard, M. S. Islam, P. R. Slater, *Journal of Materials Chemistry* **2003**, 13, 1956.
- [14] L. Leon-Reina, E. R. Losilla, M. Martínez-Lara, M. C. Martín-Sedeno, S. Bruque, P. Nunez, D. V. Sheptyakov, M. A. G. Aranda, *Chemistry of Materials* **2005**, 17, 596.
- [15] E. Kendrick, M. S. Islam, P. R. Slater, *Chemical Communications* **2008**, 715.
- [16] M. S. Islam, J. R. Tolchard, P. R. Slater, *Chemical Communications* **2003**, 1486.
- [17] J. E. H. Sansom, D. Richings, P. R. Slater, *Solid State Ionics* **2001**, 139, 205.
- [18] S. S. Pramana, W. T. Klooster, T. J. White, *Acta Cryst. B* **2007**, 63, 597.
- [19] E. Kendrick, A. Orera, P. R. Slater, *Journal of Materials Chemistry* **2009**, 19, 7955.
- [20] R. Ali, M. Yashima, Y. Matsushita, H. Yoshioka, K. Ohoyama, F. Izumi, *Chemistry of Materials* **2008**, 20, 5203.
- [21] J. R. Tolchard, P. R. Slater, *Journal of Physics and Chemistry of Solids* **2008**, 69, 2433.
- [22] K. Imaizumi, K. Toyoura, A. Nakamura, K. Matsunaga, *Solid State Ionics* **2014**, 262, 512.
- [23] K. Matsunaga, K. Toyoura, *Journal of Materials Chemistry* **2012**, 22, 7265.
- [24] T. An, T. Baikie, A. Orera, R. O. Piltz, M. Meven, P. R. Slater, J. Wei, M. L. Sanjuán, T. J. White, *Journal of the American Chemical Society* **2016**, 138, 4468.
- [25] P. M. Panchmatia, A. Orera, G. J. Rees, M. E. Smith, J. V. Hanna, P. R. Slater, M. S. Islam, *Angewandte Chemie International Edition* **2011**, 50, 9328.
- [26] Y. Nojiri, S. Tanase, M. Iwasa, H. Yoshioka, Y. Matsumura, T. Sakai, *Journal of Power Sources* **2010**, 195, 4059.
- [27] T. Baikie, P. H. J. Mercier, M. M. Elcombe, J. Y. Kim, Y. Le Page, L. D. Mitchell, T. J. White, P. S. Whitfield, *Acta Cryst. B* **2007**, 63, 251.
- [28] T. J. White, Z. L. Dong, *Acta Cryst. B* **2003**, 59, 1.

- [29] L. León-Reina, M. C. Martín-Sedeno, E. R. Losilla, A. Cabeza, M. Martínez-Lara, S. Bruque, F. M. B. Marques, D. V. Sheptyakov, M. A. G. Aranda, *Chemistry of Materials* **2003**, 15, 2099.
- [30] S. S. Pramana, W. T. Klooster, T. J. White, *Journal of Solid State Chemistry* **2008**, 181, 1717.
- [31] S. D. Findlay, N. Shibata, H. Sawada, E. Okunishi, Y. Kondo, Y. Ikuhara, *Ultramicroscopy* **2010**, 110, 903.
- [32] Y. J. Kim, R. Z. Tao, R. F. Klie, D. N. Seidman, *Acs Nano* **2013**, 7, 732.
- [33] Q. He, R. Ishikawa, A. R. Lupini, L. Qiao, E. J. Moon, O. Ovchinnikov, S. J. May, M. D. Biegalski, A. Y. Borisevich, *ACS Nano* **2015**, 9, 8412.
- [34] J. T. Mefford, X. Rong, A. M. Abakumov, W. G. Hardin, S. Dai, A. M. Kolpak, K. P. Johnston, K. J. Stevenson, *Nat Commun* **2016**, 7.
- [35] S. Kobayashi, S. D. Findlay, N. Shibata, T. Mizoguchi, Y. Sato, E. Okunishi, Y. Ikuhara, T. Yamamoto, *Applied Physics Letters* **2012**, 100, 193112.
- [36] T. An, T. Baikie, M. Weyland, J. F. Shin, P. R. Slater, J. Wei, T. J. White, *Chemistry of Materials* **2015**, 27, 1217.
- [37] Y. Zhang, Z. Su, A. K. Azad, W. Zhou, J. T. S. Irvine, *Advanced Energy Materials* **2012**, 2, 316.
- [38] J. Canales-Vázquez, M. J. Smith, J. T. S. Irvine, W. Zhou, *Advanced Functional Materials* **2005**, 15, 1000.
- [39] H. M. Rietveld, *Journal of Applied Crystallography* **1969**, 2, 65.
- [40] L. León-Reina, E. R. Losilla, M. Martínez-Lara, S. Bruque, M. A. G. Aranda, *Journal of Materials Chemistry* **2004**, 14, 1142.
- [41] E. Okunishi, H. Sawada, Y. Kondo, *Micron* **2012**, 43, 538.
- [42] E. Carlino, V. Grillo, *Physical Review B* **2005**, 71.
- [43] H. E. K. E. MacArthur, T. J. Pennycook, E. Okunishi, A. J. D'Alfonso, N. R. Lugg, L. J. Allen, P. D. Nellist, *Ultramicroscopy* **2013**, 133, 109.
- [44] A. Rosenauer, T. Mehrtens, K. Mueller, K. Gries, M. Schowalter, P. V. Satyam, S. Bley, C. Tessarek, D. Hommel, K. Sebald, M. Seyfried, J. Gutowski, A. Avramescu, K. Engl, S. Lutgen, *Ultramicroscopy* **2011**, 111, 1316.
- [45] T. Thao Tran, H. Yu, J. M. Rondinelli, K. R. Poeppelmeier, P. S. Halasyamani, *Chemistry of Materials* **2016**.
- [46] L. León-Reina, J. M. Porras-Vazquez, E. R. Losilla, M. A. G. Aranda, *Journal of Solid State Chemistry* **2007**, 180, 1250.
- [47] E. J. Abram, C. A. Kirk, D. C. Sinclair, A. R. West, *Solid State Ionics* **2005**, 176, 1941.
- [48] J. T. S. Irvine, D. C. Sinclair, A. R. West, *Advanced Materials* **1990**, 2, 132.
- [49] H. Arikawa, H. Nishiguchi, T. Ishihara, Y. Takita, *Solid State Ionics* **2000**, 136, 31.
- [50] K. S. Wallwork, B. J. Kennedy, D. Wang, *AIP Conference Proceedings* **2007**, 879, 879.
- [51] K.-D. Liss, B. Hunter, M. Hagen, T. Noakes, S. Kennedy, *Physica B: Condensed Matter* **2006**, 385–386, Part 2, 1010.
- [52] A. A. Coelho, J. S. O. Evans, I. R. Evans, A. Kern, S. Parsons, *Powder Diffraction* **2011**, 26, S22.
- [53] J. S. O. Evans, multitopas, FORTRAN 77 routine Durham University, **1999**.
- [54] K. M. Ok, E. O. Chi, P. S. Halasyamani, *Chemical Society Reviews* **2006**, 35, 710.
- [55] E. J. Kirkland, *Advanced Computing in Electron Microscopy, Second Ed*, 2010.